International Journal on Magnetic Particle Imaging
Vol 6, No 1, Article ID 2003001, 8 Pages

Infinite Science Publishing

*Research Article*

# 3D-Printing with Incorporated Iron Particles for Magnetic Actuation and MPI

Anna C. Bakenecker[a,*] · Anselm von Gladiss[a] · Thomas Friedrich[a] · Thorsten M. Buzug[a]

[a]Institute of Medical Engineering, University of Lübeck, Lübeck, Germany
*Corresponding author, email: {bakenecker,buzug}@imt.uni-luebeck.de

Received 24 October 2018; Accepted 01 January 2020; Published online 02 March 2020



**Abstract**

Magnetic particle imaging (MPI) scanners cannot only be used to image the distribution of magnetic nanoparticles, but the magnetic fields also facilitate to actuate magnetic devices. This enables the dual use of MPI scanners for simultaneous actuation and visualization of magnetic objects. It is of great interest for a variety of medical applications to magnetically steer devices, such as catheters or capsule endoscopes. Endoscopic capsules, which are driven by the natural peristaltic movements, are already in clinical routine. However, they cannot be used for the investigation of the stomach, since the capsules cannot be steered. Hence, steerable magnetic capsules can be used to endoscopically investigate the whole gastrointestinal tract, to take a biopsy or to deliver drugs locally. The 3D tomographic localization of such steerable capsules is an open task, but it is essential to localize detected abnormalities for subsequent treatments. Since MPI provides tomographic real-time images of magnetic material, it seems to be beneficial to visualize the actuation process with MPI. In this work, a material for additive manufacturing is investigated, which consists of polylactide with incorporated iron powder of µm-sized particles. The material is analyzed by light microscopy, vibrating sample magnetometry and magnetic particle spectrometry. Then the feasibility to actuate and visualize macroscopic devices made of this material inside an MPI scanner is shown. The fabricated object has a length of about 2 cm and can be rotated when applying sinusoidal currents to the focus field coils of an MPI scanner. In addition, the objects' shape led to a forward velocity in water. The suitability of the 3D-printing material for MPI is shown and static 3D images are presented.

## I. Introduction

Magnetic actuation of medical devices, such as catheters, screws or endoscopic capsules, which can be directed towards the region of interest, are of great interest for minimally invasive surgery. An actuation system is already commercially available, which consists of permanent magnets to steer catheters (Stereotaxis Inc, St. Louis, USA). Swallowable capsule endoscopes were introduced in 2000 [1] for the inspection of the small bowel and are now in clinical use. However, these approximately 3 cm long and 1 cm thick capsules are driven only by the natural peristaltic movements and are not steerable. Hence, abnormal changes may be missed. Furthermore, the exploration of the stomach is impossible and still done by tethered gastroscopy causing discomfort for the patient.

Therefore, it is advantageous to control the movement of the capsule, e.g. by external magnetic fields. A first approach was presented in 2006 [2]. A magnet was integrated into a commercially available endoscopy capsule and maneuvered by handheld permanent magnets from the outside of the patients' body. Later, a steerable capsule and an actuation system was jointly developed by Olympus Medical Systems Corporation and Siemens Healthcare [3]. Besides video cameras, steerable capsules can be also equipped with biopsy needles or sen-

sors measuring e.g. the pH-value, the temperature or the hemoglobin concentration [4–7]. For local treatments, capsules can be filled with therapeutics for the administration of drugs to the region of interest, causing a reduction of the systemic dosage [8] or thermotherapy can be applied locally [9].

The monitoring of the actuation process of untethered capsules is essential. Non tomographic imaging techniques such as video recording are sufficient for *in-vitro* experiments. Tomographic imaging techniques such as hall sensor arrays, MRI [10] or x-ray based imaging modalities [11] enable to localize endoscopic capsules *in-vivo*.

To visualize the actuation process with magnetic particle imaging (MPI) opens a new opportunity with great potential, since MPI is a radiation-free, tomographic 3D real-time imaging technique of high resolution. Usually, MPI images the concentration of superparamagnetic nanoparticles used as tracer material [12]. However, also micrometer sized magnetic particles and particles incorporated into a solid matrix are visible with MPI, even though their performance is not optimal [13, 14]. Therefore, it is also possible to visualize devices, such as catheters or swimmers which are coated with magnetic nanoparticles [15–17]. Further, MPI is advantageous, since the magnetic fields of MPI scanners can also be used to actuate magnetic objects and no imaging system needs to be integrated into an actuation setup. In an MPI scanner either the gradient of the selection field or the homogeneous focus fields can generate a force or a torque, respectively and enable the actuation inside an MPI scanner [16–23].

For medical applications in smaller cavities, such as the vascular system, the actuation and visualization of a millimeter sized swimmer inside an MPI scanner was presented [17]. A 3D-printed swimmer made of non magnetic material was painted with a lacquer mixed with magnetic nanoparticles. The actuation of this swimmer through a Y-shaped vessel phantom could be shown. Here, a new opportunity is shown, which makes a coating unnecessary, because the whole object is made of magnetic 3D-printing material. Since more material per object volume contributes to the magnetic moment, larger forces are expected. That is essential for larger objects steerable through larger cavities, such as the gastrointestinal tract. The printing material, which is used for the manufacturing of the swimming device, is analyzed. The steerability with rotating focus fields of an MPI system is investigated as well as the suitability to visualize the material with MPI, which would enable the tracking of the 3D-printed devices with MPI.

# II. Theory

Typically, MPI scanners feature three magnetic field topologies: First, a drive field to excite the magnetic particles. Second, a selection field for spatial encoding forming either a field free point or a field free line. Only particles nearby the field free region contribute to the particle signal. Third, a focus field, which is a homogeneous offset field, enabling to shift the field of view. The size of the field of view is defined by the drive field amplitude and the gradient strength [12, 24].

Two of these afore mentioned magnetic fields can generate a force on a magnetic object: The selection field can be utilized to induce a force in the direction of the field gradient pointing towards the highest magnetic field strength away from the field free region:

$$\vec{F}(\vec{r}) = \nabla\left(\vec{m}(\vec{r}) \cdot \vec{B}_S(\vec{r})\right) \tag{1}$$

with $\vec{m}(\vec{r})$ the magnetic moment and $\vec{B}_S(\vec{r})$ the selection field at a spatial position $\vec{r}$.

Further, the focus field induces a magnetic torque on the object, i.e. the objects' magnetic moment aligns with the direction of the applied magnetic field. The torque $\vec{T}(\vec{r})$ depends on the applied magnetic field $\vec{B}_F(\vec{r})$ and the magnetic moment of the object $\vec{m}(\vec{r})$:

$$\vec{T}(\vec{r}) = \vec{m}(\vec{r}) \times \vec{B}_F(\vec{r}). \tag{2}$$

When sinusoidal currents are applied to the focus field coils with a phase shift of 90° a homogeneous rotating magnetic field can be produced, such that the field vector of $\vec{B}_F$ is circularly moving and $\vec{m}$ follows this movement. The magnetic object rotates with the same frequency as the magnetic field within a certain frequency range. In order to move screws or other helical structures around their long axis pointing in e.g. x-direction, sinusoidal currents, generating a magnetic field of the same amplitude, need to be applied to the focus field coils in y- and z-direction with a 90° phase shift, respectively. Such rotating focus fields are used to show the actuation of the presented 3D printed object here.

# III. Materials and Methods

## III.I. Analysis of the Printing Material

The material under investigation is a polylactide with incorporated iron particles (Iron PLA, Proto Pasta, Vancouver, USA). The manufacturer states it is a polylactide with about 44 wt% iron powder. The objects are manufactured with a 3D-printer (Ultimaker 3, Geldermalsen, Netherlands). For the inspection under light microscopy (IX81, Olympus, Hamburg, Deutschland) one single layer with a thickness of 0.2 mm of the material was printed. In order to investigate whether the direction of printing has an impact, cylinders were manufactured one in an

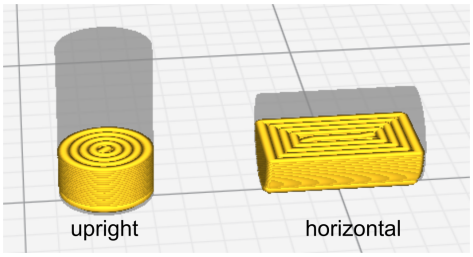


**Figure 1:** The cylinders used for VSM and MPS measurements as well as for the system matrix acquisition are printed with iron PLA. In order to investigate the impact of the printing direction one cylinder was printed in an upright position, such that the printing layers are perpendicular to the cylinder axis and filled circularly (left). A second cylinder is printed in horizontal position, such that the printing layers are parallel to the cylinder axis (right).

upright position and one in a horizontal position (see Figure 1) with a size of 3 mm diameter and 5 mm height. For the analysis by vibrating sample magnetometry (VSM) (8607 VSM System, Lake Shore Cryotronics, Inc., Westerville, Ohio, USA) a magnetic field of up to 2.5 T was applied to the cylindrical shaped samples. Measurements were performed for both cylinders with an applied magnetic field parallel and perpendicular to the cylinder axis. Further, those samples were analyzed by a magnetic particle spectrometer (MPS) with one-dimensional excitation to investigate the dynamic hysteresis curve [25]. An excitation field of 12 mT and 25 kHz was applied. The excitation direction is along the cylinder axis. In addition amplitude spectra were acquired with a spectrometer capable of three-dimensional excitation [26]. The cylindrical objects were excited along and perpendicular to the cylinder axis, subsequently. Excitation fields of 12 mT and about 25 kHz were applied.

## III.II. The Swimmer

The fabricated object has a savonius shape with a rectangular head (see Figure 2). The shape of the head was chosen to enlarge the magnetic moment perpendicular to the long axis of the swimmer. The savonius shape was invented as wind turbines by Sigurd Savonius [27]. Today, different variations are used for water turbines and wind mill rotors. A two wing, helical savonius shape was chosen. This shape has already been used and proven to be suitable for a forward velocity in water for a swimmer of millimeter size [17]. The object under investigation has a diameter of 6 mm and a length of 18 mm.

## III.III. Visualization

The suitability of the printing material for the use in MPI was investigated with an MPI scanner (MPI System 25/20FF, Bruker BioSpin, Ettlingen, Germany) by acquiring an amplitude spectrum with 3D excitation. The swimmer was placed in the MPI scanner on a sample holder. To further enhance the sensitivity of the scanner, a gradiometric receive coil was used as an additional insert for the x-receive channel [28]. To qualitatively compare the signal of the printing material to a standard MPI tracer sample, an amplitude spectrum of 10 µl undiluted Perimag (Micromod, Rostock, Germany) was acquired. A 12 mT excitation field amplitude in each direction, 2.5 T m$^{-1}$ gradient strength and 500 receive signal averages were applied. To correct for background disturbances of the scanner an empty measurement has been subtracted.

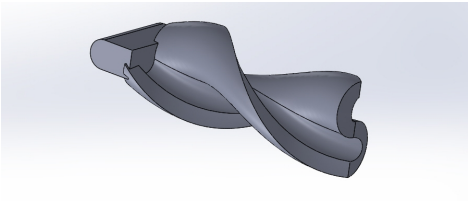

**Figure 2:** CAD-model of the savonius shaped swimmer. The swimmer is 3D-printed with magnetic print material having a length of 18 mm and a diameter of 6 mm.

For image acquisition a field gradient of 2 T m$^{-1}$ in z-direction (1 T m$^{-1}$ in x- and y-direction, respectively), and a drive field strength of 12 mT were applied, corresponding to a field of view of 24×24×12 mm$^3$. 500 receive signal averages led to a scanning time of 10 s. 3D images of the swimmer were reconstructed with a 29 × 15 × 15 system matrix of 1 mm$^3$ voxel size. A robot based system matrix acquisition was performed, by using one of the printed cylinders. The swimmer was moved in all spatial directions with a robot. A step size of 3.33 mm between each position is applied and images at 27 different sample positions were acquired. To show the suitability of tracking the device location a center of mass (CoM) was calculated from the images according to

$$\vec{r}_{\mathrm{CoM}} = \frac{\sum_{i=1}^{n} I(\vec{r}_i)\cdot \vec{r}_i}{\sum_{i=1}^{n} I(\vec{r}_i)}, \tag{3}$$

with $I$ the gray value intensity at a spatial position $\vec{r}$ of a pixel and $n$ the number of pixels in the 3D image.

## III.IV. Actuation

The swimmer is placed in a water filled silicon tube with a diameter of 7 mm. The tube was positioned in the middle of the MPI scanner (MPI System 25/20FF, Bruker BioSpin, Ettlingen, Germany) in the direction of the bore axis (x-direction). Sinusoidal currents with a 90° phase shift were applied in y- and z-direction to the focus field coils. The time dependent magnetic field then reads

$$\vec{B}_F(t) = \begin{pmatrix} 0 \\ \pm B_F^y \cos(2\pi f_F t) \\ -B_F^z \sin(2\pi f_F t) \end{pmatrix} \tag{4}$$

10.18416/ijmpi.2020.2003001

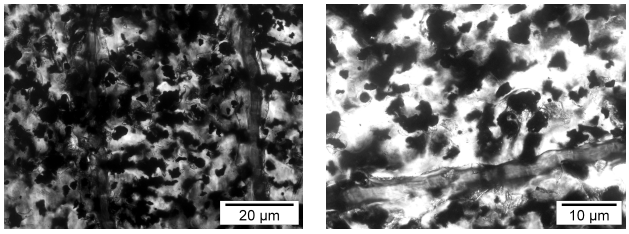


**Figure 3:** Microscopy images of one printing layer of iron PLA.

with $B_F^{y/z} = 18\,\mathrm{mT}$ the maximum focus field strength and $f_F$ the focus field frequency. The "±" in the y-component corresponds to a rotation direction of the field vector, which is either clockwise or counterclockwise. Maximal focus field amplitude was applied and frequencies of 1 Hz, 2 Hz and 3 Hz. The movement of the swimmer was observed with a video camera positioned inside the scanner bore below the setup.

# IV. Results

## IV.I. Analysis of the Printing Material

In Figure 3 pictures of the printing material taken with the light microscope can be seen. The transition between two printing rows is visible, as well as the particles, which are homogeneously incorporated into the transparent PLA and are much smaller than one printing row.

The VSM measurements can be seen in Figure 4. The results are shown for both cylinders, with the magnetic field applied perpendicular and parallel to the cylinder axis. The magnetization does not show a hysteresis effect with regard to the displayed measurement range. Saturation magnetization is reached at about 0.8 T. It can be observed, that the slope of the magnetization curves differ between the applied magnetic field directions.

In Figure 5 the dynamic magnetization curves for the cylinders of different printing directions can be seen. Both cylinders show a dynamic hysteresis. Their magnetization behavior is almost linear within the applied excitation field strength. The horizontally printed cylinder shows a steeper magnetization curve.

In Figure 6 the odd harmonics of the amplitude spectra are shown, acquired with the spectrometer capable of three-dimensional excitation. For an applied excitation field in the direction of the cylinder axis the signal amplitude is larger for the horizontal printing. If the excitation field is applied perpendicular to the cylinder axis, the signal amplitude is larger for the cylinder printed upright. Higher harmonics are distinguishable from the background beyond the 50$^{\mathrm{th}}$ harmonic.

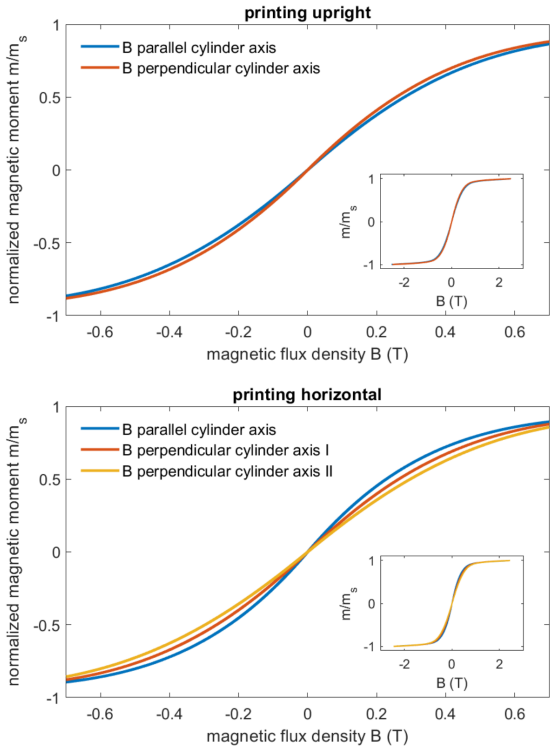


**Figure 4:** VSM measurements of two cylinder samples, which were printed in the upright position (top) and the horizontal position (bottom). The magnetic moment is normalized to the saturated magnetic moment. The magnetic field is parallel or perpendicular to the cylinder axis. For the horizontally printed sample the magnetic field was applied perpendicular to the cylinder axis once parallel to the printing layers (I) and once perpendicular to the printing layers (II).

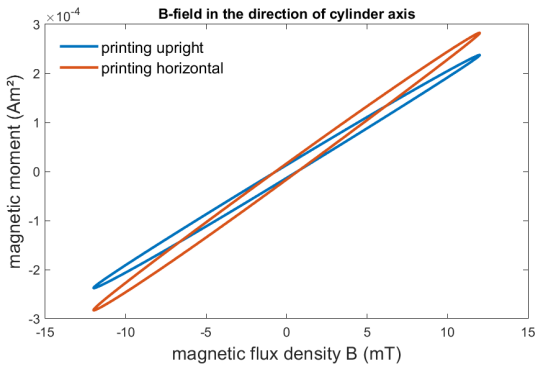


**Figure 5:** The dynamic hysteresis curve, acquired by an MPS with one dimensional excitation of 12 mT amplitude and a frequency of 25 kHz.

## IV.II. Visualization

In Figure 7 the amplitude spectrum of the swimmer can be seen in comparison to Perimag. An empty measurement was subtracted from the received signals. The displayed background signal is the subtraction of two empty

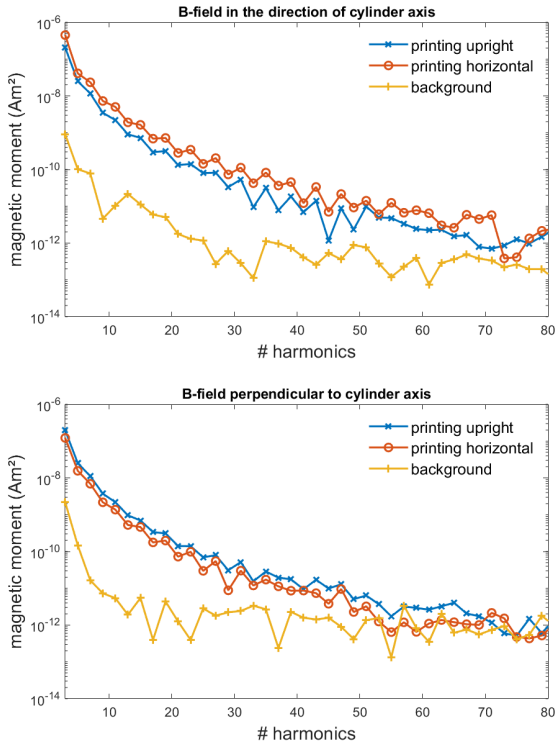


**Figure 6:** The odd harmonics of the amplitude spectra. The measurements were performed with an MPS featuring three-dimensional excitation. The results are shown for an excitation field parallel to the cylinder axis (top) and perpendicular to the cylinder axis (bottom) for two different printing directions.

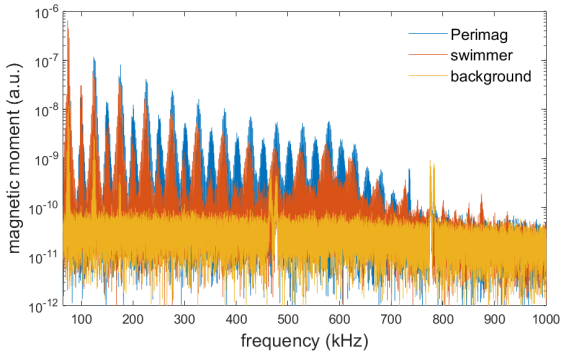


**Figure 7:** The amplitude spectrum of the 3D-printed magnetic swimmer in comparison to 10 µl undiluted Perimag. The receive channel in the x-direction of the MPI scanner is displayed, to which the gradiometric receive coil is connected.

measurements. The amplitudes of the 3D-printed magnetic swimmer are smaller compared to Perimag, but mixing frequencies corresponding to the approximately $25^{\text{th}}$ harmonic are clearly distinguishable from the background. It can be seen that the harmonics of even numbers are smaller than those of odd numbers. This phenomenon is more distinctive for the swimmer than for the particle sample.

In Figure 8 the reconstructed images of the swimmer can be seen, a sagittal, a coronal and a transversal slice are shown for three positions of the swimmer, when it was moved in x-direction. The CoM calculation for 27 different object positions is displayed in Figure 9. A threshold of 25 % was applied to the intensity values. The comparison with the known robot position, gives a mean deviation of 0.9 mm and a maximum deviation of 2.3 mm between the calculated CoM and the expected position. The object position may differ from the position calibrated by the system matrix due to misplacement of the object in the sample holder. Therefore, the center position of the object has been calibrated for each direction using the reconstructed images displaying the object at the robot's zero-position. These CoMs have been averaged and were then subtracted from all the calculated CoMs as a global offset. A mean standard deviation of 0.48px was found for the determination of the center position for each spatial direction.

### IV.III. Actuation

The swimmer is able to fulfill full rotation inside the MPI scanner, when applying the maximum focus field strengths at frequencies of 1 Hz and 2 Hz. A velocity of about 0.8 mm/s in axial direction for $f_F = 2\,\text{Hz}$ could be achieved (see Figure 10). The axial displacement for $f_F = 1\,\text{Hz}$ was very minor. The swimmer could only follow the rotation of the magnetic field for maximum field strengths and low frequencies. To maximize the magnetic force on the swimmer only maximal field strength was applied, since it was observed that smaller field strength e.g. 10 mT did not move the swimmer. At a frequency of 3 Hz the swimmer did not perform full rotation anymore, thus larger frequencies were not applied.

## V. Discussion

For the production of cm-sized swimmers a 3D-printing material containing iron powder was used. The microscopy images of the material show a homogeneous distribution of micrometer sized particles, having an irregular shape and being of different sizes (see Figure 3). The iron particles are embedded in a polylactide. The material does not show a measurable conductivity, which was proved with a multimeter measurement. The VSM measurements do not show a noticeable hysteresis effect, neither when applying the magnetic field perpendicular nor parallel to the objects' cylinder axis (see Figure 4). Different slopes of the magnetization curves can be observed, leading to the assumption that anisotropy is present, which depend on the printing layer directions.

The dynamic magnetization curves however show a significant hysteresis (see Figure 5). Since the parti-

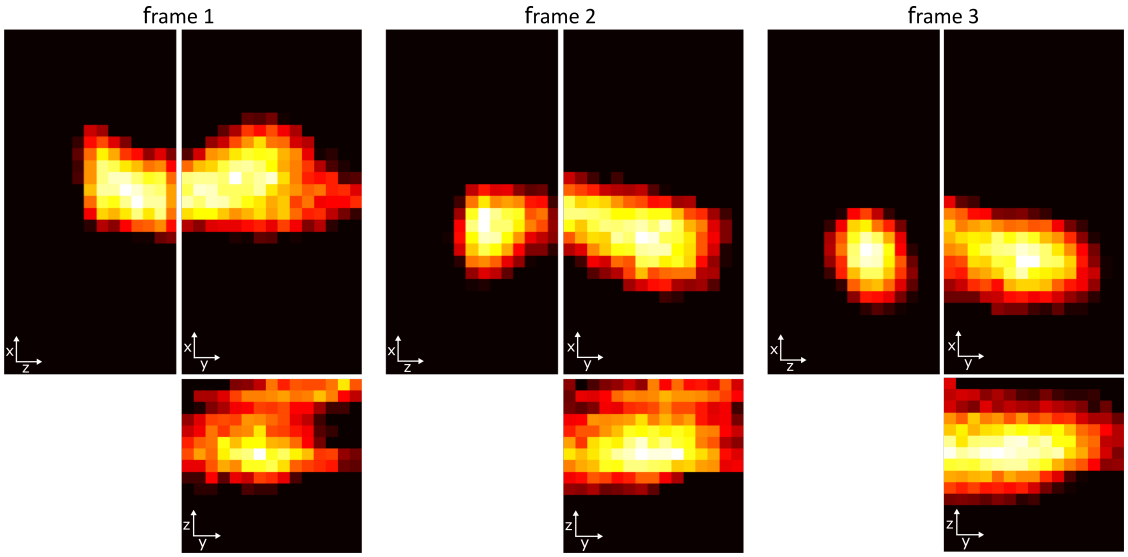


**Figure 8:** Reconstructed projection images of the swimmer. The coronal (x-y), the axial (y-z) and the sagittal (x-z) images are shown, reconstructed with a $29 \times 15 \times 15$ system matrix. The object was moved in x-direction with a robot.

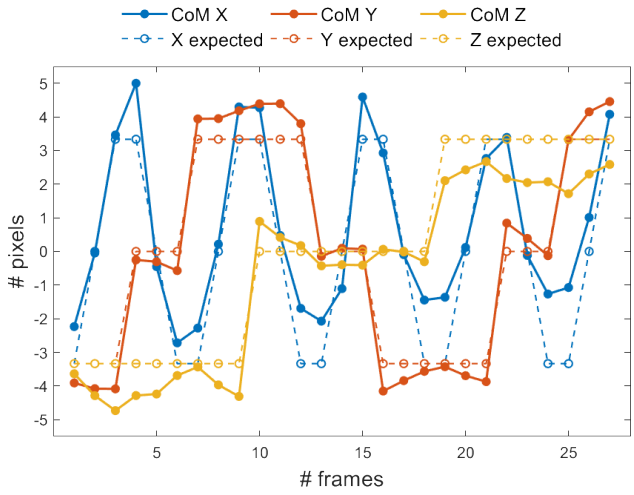


**Figure 9:** The movement of the object is evaluated by a center of mass (CoM) calculation of the reconstructed images (see Figure 8) and compared to the expected position, known from the robot position.

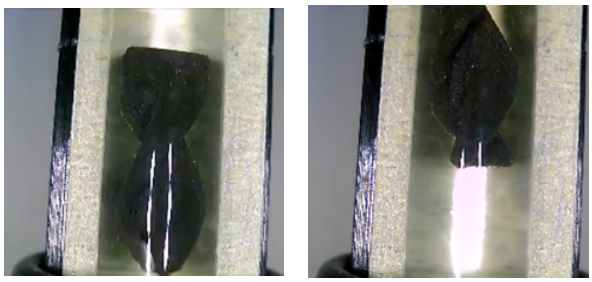

**Figure 10:** The 3D-printed swimmer in a water filled phantom inside the MPI scanner. The savonius shaped swimmer performed full rotation at frequencies of $f_F = 1\,\text{Hz}$ and $2\,\text{Hz}$ when applying a field amplitude of 18 mT. An axial movement of about 8 mm was observed when applying $f_F = 2\,\text{Hz}$ and 20 turns, which is equal to a forward velocity of 0.8 mm/s.

cles are large compared to nanoparticles usually used for MPS and MPI measurements, the relaxation of the magnetic moment is slow leading to a dynamic hysteresis. It is expected that the Brownian rotation of the particles is suppressed, since they are very large and are fixed in the polylactide matrix, which prevents a geometrical particle rotation. Further, a difference between the printing directions can be seen. A larger magnetization can be achieved for the horizontally printed cylinder. It can be concluded that the excitation along the printing direction is easier. As seen in the VSM measurements, saturation magnetization is reached at a flux density of about 0.8 T. Hence, the saturation magnetization is not reached with the MPS measurement and therefore the dynamic hysteresis does not show a non-linear magnetization behavior, which is essential for signal generation in MPI. Compared to superparamagnetic iron-oxide particles, typically used in MPI, the signal amplitude of the iron-PLA is therefore expected to be lower.

The measurements performed with the multi-dimensional MPS show that the signals' amplitudes are larger when the excitation field is applied in the same direction as the printing layer's orientation.

In the amplitude spectrum of the swimmer acquired with the MPI scanner multiple mixing frequencies are clearly distinguishable from the background (see Figure 7). In Figure 8 the swimmer is clearly visible in the axial, sagittal and coronal slice of the 3D MPI images. However, the shape of the swimmer, which is oriented with its long axis in x-direction cannot be represented.

10.18416/ijmpi.2020.2003001

The reconstructed images show a tilted broadening in y-direction. It is not clear, where this artifact comes from. The system matrix was acquired with one of the cylinder samples. These samples are much bigger than typically used point samples, therefore it was expected that the quality of the reconstruction is limited, but the manufacturing of smaller devices was not feasible. Since the signal depends on the printing and excitation direction, it is possible that the signal differs depending on the shape of the object. Then, the system matrix is not perfectly adequate for reconstruction and artifacts may occur. The center of mass calculation showed the feasibility to track the position of the swimmer. An average accuracy could be calculated from 27 evaluated images and was found to be 0.9 mm.

It could be shown that the magnetic torque inside an MPI scanner is sufficient to continuously rotate the swimmer by applying sinusoidal currents to the focus field coils, when generating maximum flux density and applying frequencies of 1 Hz or 2 Hz. At higher frequencies the viscous friction acting against the magnetic torque becomes larger and prevents full rotation of the swimmer or the magnetic moment of the swimmer may not follow the rotating magnetic field anymore. The savonius shape led to an axial movement of the swimmer in water. The fluid dynamic properties of the swimmer are not yet optimized. Most probably, a better axial movement can be achieved by optimizing the swimmer's shape. It is supposed that the savonius shape is preferable for large objects, i.e. for swimmer dynamics at large Reynolds numbers. This can be conjectured since the savonius shape is known for wind turbins and rotors, where turbulent flow dynamics are present. Whereas the flow dynamics of micrometer sized objects is laminar, low Reynolds numbers are applicable. Most micrometer sized swimmers feature a helical shape [29–31].

Further steps are the additional use of the selection field, such that the field free point moves around the object [20]. This enables to selectively actuate swimmers and more sophisticated phantoms containing more tubes and different directions could be used. For achieving more propulsion, different shapes are of future investigation. The used printing technique is suitable for large objects, but the resolution of the used 3D-printer is limited, hence smaller objects cannot be produced.

# VI. Conclusion

It could be shown that the fabrication of a swimmer of centimeter size is possible with a printing material with incorporated iron particles. The materials' magnetic properties were investigated by light microscopy, VSM and MPS. The presented object is suitable for magnetic actuation and can be visualized with MPI. It reacts to an applied rotating magnetic field of an MPI scanner and followed the rotation for low frequencies. Due to the swimmers' shape a forward movement in water can be observed. The analysis of the 3D printing material showed a non optimal, but suitable performance of the material for MPI, compared to standard MPI tracers. Static 3D images of the swimmer were acquired, paving the way towards monitoring the actuation process of magnetic objects with MPI. The size of the swimmer is reasonable for a future medical application inside the gastrointestinal tract.

# Acknowledgments

Funding by the Federal Ministry of Education and Research, Germany (BMBF) under grant numbers 13GW0069A, 13GW0230B, 01DL17010A and 13GW0071D is gratefully acknowledged.

# References

[1] G. Iddan, G. Meron, A. Glukhovsky, and P. Swain. Wireless capsule endoscopy. *Nature*, 405(6785):417–417, 2000, doi:10.1038/35013140.

[2] F. Carpi, S. Galbiati, and A. Carpi. Magnetic shells for gastrointestinal endoscopic capsules as a means to control their motion. *Biomedicine & Pharmacotherapy*, 60(8):370–374, 2006, doi:10.1016/j.biopha.2006.07.001.

[3] J. Rey, H. Ogata, N. Hosoe, K. Ohtsuka, N. Ogata, K. Ikeda, H. Aihara, I. Pangtay, T. Hibi, S. Kudo, and H. Tajiri. Feasibility of stomach exploration with a guided capsule endoscope. *Endoscopy*, 42(07):541–545, 2010, doi:10.1055/s-0030-1255521.

[4] S. Park, K.-i. Koo, S. M. Bang, J. Y. Park, S. Y. Song, and D. D. Cho. A novel microactuator for microbiopsy in capsular endoscopes. *Journal of Micromechanics and Microengineering*, 18(2):025032, 2008, doi:10.1088/0960-1317/18/2/025032.

[5] M. Simi, G. Gerboni, A. Menciassi, and P. Valdastri. Magnetic Torsion Spring Mechanism for a Wireless Biopsy Capsule. *Journal of Medical Devices*, 7(4), 2013, doi:10.1115/1.4025185.

[6] M. Sitti, H. Ceylan, W. Hu, J. Giltinan, M. Turan, S. Yim, and E. Diller. Biomedical Applications of Untethered Mobile Milli/Microrobots. *Proceedings of the IEEE*, 103(2):205–224, 2015, doi:10.1109/JPROC.2014.2385105.

[7] D. Son, H. Gilbert, and M. Sitti. Magnetically Actuated Soft Capsule Endoscope for Fine-Needle Biopsy. *Soft Robotics*, 2019, doi:10.1089/soro.2018.0171.

[8] S. Yim and M. Sitti. Shape-Programmable Soft Capsule Robots for Semi-Implantable Drug Delivery. *IEEE Transactions on Robotics*, 28(5):1198–1202, 2012, doi:10.1109/TRO.2012.2197309.

 

[9] M. Sendoh, K. Ishiyama, K. Arai, M. Jojo, F. Sato, and H. Matsuki. Fabrication of magnetic micromachine for local hyperthermia. *IEEE Transactions on Magnetics*, 38(5):3359–3361, 2002, doi:10.1109/TMAG.2002.802305.

[10] G. Kósa, P. Jakab, G. Székely, and N. Hata. MRI driven magnetic microswimmers. *Biomedical Microdevices*, 14(1):165–178, 2012, doi:10.1007/s10544-011-9594-7.

[11] F. Carpi, N. Kastelein, M. Talcott, and C. Pappone. Magnetically Controllable Gastrointestinal Steering of Video Capsules. *IEEE Transactions on Biomedical Engineering*, 58(2):231–234, 2011, doi:10.1109/TBME.2010.2087332.

[12] B. Gleich and J. Weizenecker. Tomographic imaging using the nonlinear response of magnetic particles. *Nature*, 435(7046):1214–1217, 2005, doi:10.1038/nature03808.

[13] C. Jacobi, T. Friedrich, and K. Lüdtke-Buzug. Synthesis and Characterisation of Superparamagnetic Polylactic acid based Polymers. *International Journal on Magnetic Particle Imaging*, 3(2), 2017, doi:10.18416/IJMPI.2017.1710001.

[14] J. Wells, N. Löwa, H. Paysen, U. Steinhoff, and F. Wiekhorst. Probing particle-matrix interactions during magnetic particle spectroscopy. *Journal of Magnetism and Magnetic Materials*, 475:421–428, 2019, doi:10.1016/j.jmmm.2018.11.109.

[15] J. Haegele, N. Panagiotopoulos, S. Cremers, J. Rahmer, J. Franke, R. L. Duschka, S. Vaalma, M. Heidenreich, J. Borgert, P. Borm, J. Barkhausen, and F. M. Vogt. Magnetic Particle Imaging: A Resovist Based Marking Technology for Guide Wires and Catheters for Vascular Interventions. *IEEE Transactions on Medical Imaging*, 35(10):2312–2318, 2016, doi:10.1109/TMI.2016.2559538.

[16] J. Rahmer, C. Stehning, and B. Gleich. Spatially selective remote magnetic actuation of identical helical micromachines. *Science Robotics*, 2(3):2845, 2017, doi:10.1126/scirobotics.aal2845.

[17] A. C. Bakenecker, A. von Gladiss, T. Friedrich, U. Heinen, H. Lehr, K. Lüdtke-Buzug, and T. M. Buzug. Actuation and visualization of a magnetically coated swimmer with magnetic particle imaging. *Journal of Magnetism and Magnetic Materials*, 473:495–500, 2019, doi:10.1016/j.jmmm.2018.10.056.

[18] X. Zhang, T.-A. Le, and J. Yoon. Development of a real time imaging-based guidance system of magnetic nanoparticles for targeted drug delivery. *Journal of Magnetism and Magnetic Materials*, 427:345–351, 2017, doi:10.1016/j.jmmm.2016.10.056.

[19] N. Nothnagel, J. Rahmer, B. Gleich, A. Halkola, T. M. Buzug, and J. Borgert. Steering of Magnetic Devices With a Magnetic Particle Imaging System. *IEEE Transactions on Biomedical Engineering*, 63(11):2286–2293, 2016, doi:10.1109/TBME.2016.2524070.

[20] J. Rahmer, D. Wirtz, C. Bontus, J. Borgert, and B. Gleich. Interactive Magnetic Catheter Steering With 3-D Real-Time Feedback Using Multi-Color Magnetic Particle Imaging. *IEEE Transactions on Medical Imaging*, 36(7):1449–1456, 2017, doi:10.1109/TMI.2017.2679099.

[21] J. Rahmer, C. Stehning, and B. Gleich. Remote magnetic actuation using a clinical scale system. *PLOS ONE*, 13(3):e0193546M. Dao, Ed., 2018, doi:10.1371/journal.pone.0193546.

[22] A. Bakenecker, T. Friedrich, A. von Gladiss, and T. M. Buzug, Lateral Movement of a Helical Swimmer Induced by Rotating Focus Fields in a Preclinical MPI Scanner, in *International Workshop on Magnetic Particle Imaging*, 99–100, 2018.

[23] F. Griese, T. Knopp, C. Gruettner, F. Thieben, K. Müller, S. Loges, P. Ludewig, and N. Gdaniec. Simultaneous Magnetic Particle Imaging and Navigation of large superparamagnetic nanoparticles in bifurcation flow experiments. *Journal of Magnetism and Magnetic Materials*, 498:166206, 2020, doi:10.1016/j.jmmm.2019.166206.

[24] T. Knopp and T. M. Buzug, Magnetic Particle Imaging: An Introduction to Imaging Principles and Scanner Instrumentation. Berlin, Heidelberg: Springer Berlin Heidelberg, 2012, doi:10.1007/978-3-642-04199-0.

[25] S. Biederer, T. Knopp, T. F. Sattel, K. Lüdtke-Buzug, B. Gleich, J. Weizenecker, J. Borgert, T. M. Buzug, and K. Lüdtke-Buzug. Magnetization response spectroscopy of superparamagnetic nanoparticles for magnetic particle imaging. *Journal of Physics D: Applied Physics*, 42(20):205007, 2009, doi:10.1088/0022-3727/42/20/205007.

[26] X. Chen, M. Graeser, A. Behrends, A. von Gladiss, and T. M. Buzug. First Measurement Results of a 3D Magnetic Particle Spectrometer. *International Journal on Magnetic Particle Imaging*, 4(1), 2018, doi:10.18416/IJMPI.2018.1810001.

[27] S. Savonius, The Wing-Rotor - in Theory and Practise. Savonius und Co. Helsingfors, Finnland, 1926, URL: https://www.prh.fi/stc/attachments/innogalleria/savonius_kirja.pdf.

[28] M. Graeser, T. Knopp, P. Szwargulski, T. Friedrich, A. von Gladiss, M. Kaul, K. M. Krishnan, H. Ittrich, G. Adam, and T. M. Buzug. Towards Picogram Detection of Superparamagnetic Iron-Oxide Particles Using a Gradiometric Receive Coil. *Scientific Reports*, 7(1):6872, 2017, doi:10.1038/s41598-017-06992-5.

[29] A. Ghosh and P. Fischer. Controlled Propulsion of Artificial Magnetic Nanostructured Propellers. *Nano Letters*, 9(6):2243–2245, 2009, doi:10.1021/nl900186w.

[30] S. Tottori, L. Zhang, F. Qiu, K. K. Krawczyk, A. Franco-Obregón, and B. J. Nelson. Magnetic Helical Micromachines: Fabrication, Controlled Swimming, and Cargo Transport. *Advanced Materials*, 24(6):811–816, 2012, doi:10.1002/adma.201103818.

[31] M. Medina-Sánchez, L. Schwarz, A. K. Meyer, F. Hebenstreit, and O. G. Schmidt. Cellular Cargo Delivery: Toward Assisted Fertilization by Sperm-Carrying Micromotors. *Nano Letters*, 16(1):555–561, 2016, doi:10.1021/acs.nanolett.5b04221.